GODUNOV-TYPE SOLUTIONS FOR TRANSIENT FLOWS IN SEWERS

Arturo S. León[1], Mohamed S. Ghidaoui, M. ASCE [2],

Arthur R. Schmidt, M. ASCE[3], Marcelo H. García, M. ASCE[4]

Abstract

This work is part of a long term project which aims at developing a hydraulic model for real-time simulation of unsteady flows in sewers ranging from gravity flows, to partly gravity-partly surcharged flows to fully surcharged flows. The success of this project hinges on the ability of the hydraulic model to handle a wide range of complex boundaries and to provide accurate solutions with least Central Processing Unit (CPU) time. This first paper focuses on the development and assessment of two second-order explicit Finite-Volume Godunov-Type Schemes (GTS) for unsteady gravity flows in sewers, but with no surcharging. Traditionally, hydraulic transients have been modeled using the Method of Characteristics (MOC), which is noted for its ability to handle complex boundary conditions (BCs). The two GTS described herein incorporate BCs in a similar manner to the MOC.

[1]Ph.D. Student, Dept. of Civil and Environmental Eng., University of Illinois at Urbana-Champaign, Urbana, Illinois 61801, USA. Phone: (217)333-6178; Fax: (217)333-0687; E-mail: asleon@uiuc.edu (corresponding author)

[2]Associate Professor, Dept. of Civil Engineering, The Hong Kong University of Science and Technology, Hong Kong. Phone: (852)2358-7174; Fax: (852)2358-1534; E-mail: ghidaoui@ust.hk

[3]Research Assistant Professor, V.T. Chow Hydrosystems Lab., Dept. of Civil and Envir. Eng., University of Illinois at Urbana-Champaign, Urbana, IL 61801, USA. Phone: (217)333-4934; Fax: (217)333-0687; E-mail: aschmidt@uiuc.edu

[4]Chester and Helen Siess Professor and Director, V.T. Chow Hydrosystems Lab., Dept. of Civil and Envir. Eng., University of Illinois at Urbana-Champaign, Urbana, IL 61801, USA. Phone: (217)244-4484; Fax: (217)333-0687; E-mail: mhgarcia@uiuc.edu

The accuracy and efficiency of these GTS schemes are investigated using problems whose solution contain features that are relevant to transient flows in sewers such as shock, expansion and roll waves. The results show that these GTS schemes are significantly faster to execute than the fixed-grid MOC scheme with space-line interpolation, and in some cases, the accuracy produced by the two GTS schemes cannot be matched by the accuracy of the MOC scheme, even when a Courant number close to one and a large number of grids is used. Furthermore, unlike the MOC solutions, which exhibit increasing numerical dissipation with decreasing Courant numbers, the resolution of the shock fronts was maintained by the GTS schemes even for very low Courant numbers (0.001).
CE Database Keywords: Gravity sewers; Hydraulic transients; Sewer pipes; Shallow water; Shock waves; Unsteady flow; Water Waves.

Introduction

One of the most important considerations for successful implementation of real-time control is development of efficient models to provide real-time simulation of the system and short-term prediction of the conditions that will result from various control decisions (Schilling 1996; Duchesne et al. 2004). The computational speed or efficiency of sewer models is a critical factor for real-time control, since several simulations are required within a control loop in order to optimize the control strategy, and where small simulation time steps are needed to reproduce the rapidly varying hydraulics. Because of this requirement, many of the models used for real-time control of combined sewer systems incorporate simplifying assumptions that enhance computational speed at the expense of precision of the simulation results (e.g., Norreys and Cluckie 1997; Duchesne et al. 2004).

Although sewers are generally designed based on gravity flow, in practice large variations in the inflow and outflow from sewer systems result in flow conditions that vary from dry to gravity flow to partly gravity-partly pressurized flow (mixed flow), to fully pressurized flow. The transitions among

these flow regimes are governed by flow instabilities. Yen (1986, 2001) classified these instabilities into the following types: 1. Dry bed instability, 2. Supercritical-subcritical instability, 3. Roll wave instability 4. Open channel-pressurized flow instability and 5. Full pressurized flow instability. Some of these instabilities may lead to sewer surcharging that can in turn result in backflow and overflow of sewers, blow-off of manhole covers, and geysering. The three first instabilities are related to gravity flows, the fifth to pressurized flows, and the fourth to the transition between gravity and pressurized flows. The dry bed instability occurs when the bed is nearly dry. Flow routing through an originally dry sewer pauses a major numerical difficulty at the wet-dry interface. The usual practice is to assume that the sewer is not completely dry, but has an initial thin film of water; the depth of which depends on the capability of the numerical model (e.g., Abbott and Minns 1997). Fortunately, sewer surcharging does not often begin from dry conditions. Nevertheless, if dry conditions do occur, the practice of artificial film has been found to work well in rapid transients (e.g., Delis 2000; Tseng et al. 2001). The scope of this paper focuses only on unsteady gravity flows in sewers, and therefore is limited to only the second and third instabilities.

Unsteady gravity flows in sewers have been traditionally modeled by numerically solving the one-dimensional equations of continuity and momentum. Commonly used models range in sophistication from kinematic wave to full dynamic wave solution of these equations (Yen 2001). Most of the models that solve these equations at the level of the full dynamic wave use an implicit finite-difference scheme when the formation of transients is secondary to issues such as conveyance capacity. However, most of the models developed primarily to examine the formation of hydraulic transients use schemes based on the Method Of Characteristics (MOC). The MOC can easily handle complex boundary conditions, however, interpolations necessary for Courant numbers less than one result in smoothing (damping) of waves and diffusion of the wave fronts; diffusion makes waves arrive earlier to the boundaries, and damping reduces the wave peak and may artificially delay the time of occurrence

of surcharging. Therefore, what is needed is a computationally efficient scheme that retains the same ability as the MOC in terms of handling boundary conditions, but provides higher resolution of waves in sewers.

Godunov Type Schemes (GTS) for the solution of shallow water equations have been the subject of considerable research (Glaister 1988; Alcrudo et al. 1992; Fujihara and Borthwick 2000; Sanders 2001; Toro 2001; Caleffi et al. 2003; Zoppou and Roberts 2003). These schemes fall within the group of Finite Volume (FV) methods that have the ability to conserve mass and momentum and to provide sharp resolution of discontinuities without spurious oscillations (Hirsch 1990). Additionally, unlike the MOC schemes, the resolution of GTS is not significantly reduced for low Courant numbers. Furthermore, the boundary conditions for these schemes are treated in a similar way to the MOC. Historically, a GTS for flows in rectangular channels was first implemented by Glaister (1988) and for non-rectangular prismatic channels by Alcrudo et al. (1992). Later, another scheme for non-prismatic channels was implemented by Sanders (2001) and applied to triangular and trapezoidal channels.

Recently, Zhao and Ghidaoui (2004) found that Riemann solutions are well suited for water-hammer flows; these authors show that the first-order GTS is identical to the MOC scheme with space-line interpolation. They also show that, for a given level of accuracy, the second-order GTS requires much less memory storage and execution time than either the first-order scheme or the MOC scheme with space-line interpolation.

Since the focus of this research is surcharging of sewers, a robust and efficient numerical model able to reproduce unsteady gravity flows, unsteady pressurized flows and the simultaneous occurrence of gravity and pressurized flows was developed by the authors. The model consists of three parts: (1) a pressurized flow model that is similar to the approach of Zhao and Ghidaoui (2004); (2) a gravity flow model that is based on the application of GTS methods to unsteady gravity flows in

sewers; and (3) an open channel-pressurized flow interface model that handles the interfaces using an adaptive grid shock tracking-capturing approach. Since to date, no specific application of GTS methods to gravity flows in sewers (circular geometry) has been reported, the objective of this paper is to formulate and apply GTS methods for gravity flows in sewers and to compare their accuracy and efficiency to MOC schemes. The scope of this first paper is limited to the application of GTS to gravity flows in sewers, but with no surcharging. The modeling of unsteady open channel-pressurized flow interfaces will be described in a subsequent paper. This paper is organized as follows: (1) the governing equations are presented in conservation-law form; (2) the corresponding integral form and FV discretization is described; (3) two Riemann solvers for the flux computation at the cell interfaces are provided; (4) a brief description for the formulation of boundary conditions is presented; (5) the stability constraints for the source term discretized using the second-order Runge-Kutta are formulated; and (6) the schemes are tested using several problems whose solution contain features that are relevant to transient flows in sewers. Finally, the results are summarized in the conclusion.

Governing Equations

One-dimensional open channel flow continuity and momentum equation for non prismatic channels or rivers may be written in its vector conservative form as follows (Chaudhry 1987):

$$\frac{\partial \mathbf{U}}{\partial t} + \frac{\partial \mathbf{F}}{\partial x} = \mathbf{S} \tag{1}$$

where the vector variable $\mathbf{U}$, the flux vector $\mathbf{F}$ and the source term vector $\mathbf{S}$ are given respectively by:

$$\mathbf{U} = \begin{bmatrix} A \\ Q \end{bmatrix}, \ \mathbf{F} = \begin{bmatrix} Q \\ \frac{Q^2}{A} + \frac{A\overline{p}}{\rho} \end{bmatrix} \text{ and } \mathbf{S} = \begin{bmatrix} 0 \\ F_w + (S_0 - S_f)gA \end{bmatrix} \tag{2}$$

where A = cross-sectional area of the channel; Q = flow discharge; $\overline{p}$ = average pressure of the water column over the cross sectional area; ρ = liquid density; g = gravitational acceleration; S_0 = slope

of the bottom channel; S_f = slope of the energy line, which may be estimated using an empirical formula such as the Manning's equation; and F_w = momentum term arising from the longitudinal variation of the channel width. For a circular cross-section channel (Figure 1), F_w becomes zero, the hydraulic area is given by $A = d^2/8(\theta - \sin\theta)$, the hydraulic radius by $R = d/4(1 - \sin\theta/\theta)$, and the term $A\overline{p}/\rho$ contained in the flux term $\mathbf{F}$ in Eq. (2) is given by

$$\frac{A\overline{p}}{\rho} = \frac{g}{12}\left[(3d^2 - 4dy + 4y^2)\sqrt{y(d-y)} - 3d^2(d-2y)\arctan\frac{\sqrt{y}}{\sqrt{d-y}}\right] \tag{3}$$

where d is the diameter of the circular cross-section channel and y is the water depth.

Formulation of Finite Volume Godunov-type schemes

This method is based on writing the governing equations in integral form over an elementary control volume or cell, hence the general term of Finite Volume (FV) method. The computational grid or cell involves the discretization of the spatial domain x into cells of length Δx and the temporal domain t into intervals of duration Δt. The ith cell is centered at node i and extends from $i - 1/2$ to $i + 1/2$. The flow variables (A and Q) are defined at the cell centers i and represent their average value within each cell. Fluxes, on the other hand are evaluated at the interfaces between cells ($i-1/2$ and $i + 1/2$). For the ith cell, the integration of Equation (1) with respect to x from control surface $i - 1/2$ to control surface $i + 1/2$ yields:

$$\frac{\partial}{\partial t}\int_{i-1/2}^{i+1/2}\mathbf{U}dx + \mathbf{F}_{i+1/2} - \mathbf{F}_{i-1/2} = \int_{i-1/2}^{i+1/2}\mathbf{S}dx \tag{4}$$

Recalling that the flow variables (A and Q) are averaged over the cell, the application of Green's theorem to Equation (4), gives:

$$\mathbf{U}_i^{n+1} = \mathbf{U}_i^n - \frac{\Delta t}{\Delta x}(\mathbf{F}_{i+1/2}^n - \mathbf{F}_{i-1/2}^n) + \frac{\Delta t}{\Delta x}\int_{i-1/2}^{i+1/2}\mathbf{S}dx \tag{5}$$

where the superscripts n and $n+1$ reflect the t and $t + \Delta t$ time levels respectively. In Equation (5), the determination of $\mathbf{U}$ at the new time step $n + 1$ requires the computation of the numerical flux

at the cell interfaces at the old time n and the evaluation of the source term. The source terms are introduced into the solution through a second-order time splitting. The evaluation of the flux term is presented in the next section.

Flux computation

In the Godunov approach, the numerical flux is determined by solving a local Riemann problem at each cell interface. The Riemann problem for a general hyperbolic system is the following initial-value problem:

$$\frac{\partial \mathbf{U}}{\partial t} + \frac{\partial \mathbf{F}}{\partial x} = 0 \tag{6}$$

$$\mathbf{U}_x^n = \begin{cases} \mathbf{U}_L^n \text{ for } x \leq x_{i+1/2} \\ \mathbf{U}_R^n \text{ for } x > x_{i+1/2} \end{cases} \tag{7}$$

For each cell interface, the states $\mathbf{U}_L^n$ and $\mathbf{U}_R^n$ are estimated from a polynomial reconstruction whose order determines the accuracy of the scheme. For Godunov's first-order accuracy method, a piecewise constant polynomial is used, whereas a second-order accuracy scheme is produced if linear interpolation is used. Higher order accuracy Godunov schemes are found using higher order polynomials. Only first-order accuracy schemes produce monotone preserving solutions (Godunov 1959), however the accuracy of these schemes in smooth regions is of order one and a very fine grid would be required to minimize numerical errors. The rate of convergence of second or higher order schemes is much better than first order schemes. Therefore, to achieve a given level of accuracy, higher order schemes require much less grid points than the first order schemes. However, higher order schemes are prone to spurious oscillations in the vicinity of discontinuities. Total Variation Diminishing (TVD) methods may be used to preserve the accuracy of the schemes away from the discontinuities and that are oscillation-free near shock waves and other sharp flow features. In this

paper, second-order accuracy in space and time is obtained by using a Monotone Upstream-centred Scheme for Conservation Laws (MUSCL) reconstruction in conjunction with a Hancock two-stage scheme for advancing the cell average solution from one time level to the next (e.g., Toro 2001). The TVD property of this method is ensured by applying the MINMOD pre-processing slope limiter (e.g., Toro 2001).

The intercell flux $\mathbf{F}_{i+1/2}$ is computed using an exact or approximate solution of the Riemann Problem. The intercell flux is then used to update $\mathbf{U}$ at the nodes. In order to reduce the computational time, the exact solution of the Riemann problem is usually replaced with an approximate one. These approximate solvers, if carefully selected, may lead to robust schemes with very good accuracy and that are simple to implement. In what follows, two efficient approximate Riemann solvers are derived for general cross-section open channel flows and then applied for circular conduits.

Guinot approximate-state Riemann solver

In this approach, the solution of the Riemann problem is approximated by an intermediate region $\mathbf{U}_\star$ of constant state separated from the left and right states $\mathbf{U}_L$ and $\mathbf{U}_R$ by two waves that may be rarefactions or shocks (Figure 2). From these three states only the intermediate state is unknown. This unknown state is obtained by assuming that the flow is continuous across these two waves (two rarefaction waves) and consequently the differential relationships provided by the generalized Riemann invariants hold across these waves. By manipulating these differential relationships across the first wave ($dx/dt = u - c$) and second wave ($dx/dt = u + c$) the following relationships are obtained (the details of the derivation are given in the appendix A):

$$u_L + \phi_L = u_\star + \phi_\star, \quad \text{across} \quad dx/dt = u - c \tag{8}$$

$$u_\star - \phi_\star = u_R - \phi_R, \quad \text{across} \quad dx/dt = u + c \tag{9}$$

where ϕ (see appendix A for derivation details) and the gravity wave celerity c are given respectively by:

$$\phi = \sqrt{g\frac{d}{8}}\left[\sqrt{3}\,\theta - \frac{\sqrt{3}}{80}\,\theta^3 + \frac{19\sqrt{3}}{448000}\,\theta^5 + \frac{\sqrt{3}}{10035200}\,\theta^7 + \frac{491\sqrt{3}}{27\times 7064780800}\,\theta^9 + ...\right] \tag{10}$$

$$c = \sqrt{g\frac{d}{8}}\sqrt{\frac{\theta - \sin\theta}{\sin\frac{\theta}{2}}} \tag{11}$$

By combining Equations (8) and (9), the flow variables in the intermediate state (star region) are obtained:

$$u_\star = \frac{u_L + u_R}{2} + \frac{\phi_L - \phi_R}{2} \tag{12}$$

$$\phi_\star = \frac{\phi_L + \phi_R}{2} + \frac{u_L - u_R}{2} \tag{13}$$

If the left or right wave is a shock, the speed of this shock (c_s) can be computed by applying the Rankine-Hugoniot condition to either the continuity or the momentum equation. This gives the following relations:

$$\begin{aligned} c_{s\ (K\,=\,L,\ R)} &= \frac{Q_\star - Q_K}{A_\star - A_K} \\ c_{s\ (K\,=\,L,\ R)} &= \frac{\frac{Q_\star^2}{A_\star} - \frac{Q_K^2}{A_K} + \frac{A_\star \overline{p}_\star}{\rho} - \frac{A_K \overline{p}_K}{\rho}}{Q_\star - Q_K} \end{aligned} \tag{14}$$

After the computation of all the wave celerities and shock speeds (if present), it is possible to determine in which region the initial discontinuity is located and thus to compute the flux. In what follows, the scheme due to Guinot (2003) is summarized:

(1) Compute $u_\star$ (or $Q_\star$) and $\phi_\star$ (or $A_\star$) using the Equations (12) and (13).

(2) Determine u (or Q) and ϕ (or A) at the interface $i+1/2$ from the following tests:

$$\begin{cases} \text{if } s_L \geq 0 \ \ \& \ \ s1_\star < 0 & \text{the first wave is a shock. The shock speed } c_s \text{ must be computed with } K = L \text{ using one of the relations given in the system of Equations (14). The solution is given by } \mathbf{U}_L \text{ if } c_s > 0 \text{ and by } \mathbf{U}_\star \text{ otherwise.} \\ \text{if } s_L \geq 0 \ \ \& \ \ s1_\star > 0 & \text{the solution is given by } \mathbf{U}_L \text{ regardless of the nature of the first wave.} \\ \text{if } s_L < 0 \ \ \& \ \ s1_\star > 0 & \text{the solution is obtained by solving Equation (8) with } u_\star = c_\star \\ \text{if } s1_\star \leq 0 \ \ \& \ \ s2_\star \geq 0 & \text{the solution is given by } \mathbf{U}_\star \\ \text{if } s2_\star < 0 \ \ \& \ \ s_R > 0 & \text{the solution is obtained by solving Equation (9) with } u_\star = -c_\star \\ \text{if } s_R \leq 0 \ \ \& \ \ s2_\star > 0 & \text{the second wave is a shock. The shock speed } c_s \text{ must be computed with } K = R \text{ using one of the relations given in the system of Equations (14). The solution is given by } \mathbf{U}_R \text{ if } c_s < 0 \text{ and by } \mathbf{U}_\star \text{ otherwise.} \\ \text{if } s_R \leq 0 \ \ \& \ \ s2_\star < 0 & \text{the solution is given by } \mathbf{U}_R \text{ regardless of the nature of the second wave.} \end{cases}$$

where $s_L = u_L - c_L$, $s1_\star = u_\star - c_\star$, $s2_\star = u_\star + c_\star$ and $s_R = u_R + c_R$.

(3) Once the flow variables (A and Q) at the interface $i+1/2$ are known, the flux at the interface is computed using the Equation 2.

HLL Approximate Riemann solver

The HLL Riemann solver takes its name from the initials of Harten, Lax and Van Leer (Toro 2001). In this approach, the solution of the Riemann problem is approximated by an intermediate region $\mathbf{U}_\star$ of constant state separated from the left and right states $\mathbf{U}_L$ and $\mathbf{U}_R$ by two infinitely thin waves (shocks). Figure 3 illustrates this approximation. In this method, the numerical flux $\mathbf{F}_{i+1/2}$ is obtained by applying the integral form of the conservation laws in appropriate control volumes

yielding:

$$\mathbf{F}_{i+1/2} = \begin{cases} \mathbf{F}_L & \text{if } s_L > 0 \\ \frac{s_R\mathbf{F}_L - s_L\mathbf{F}_R + s_R s_L(\mathbf{U}_R - \mathbf{U}_L)}{s_R - s_L} & \text{if } s_L \leq 0 \leq s_R \\ \mathbf{F}_R & \text{if } s_R < 0 \end{cases} \tag{15}$$

where s_L and s_R are the wave speed estimates for the left and right waves, respectively. It can be noticed in Equation (15) that the first and third fluxes correspond to supercritical flows moving to the right and left, respectively and the second one corresponds to a subcritical flow moving to the right or left. The wave speeds s_L and s_R are determined by eliminating $Q_\star$ in the system of Equations (14), resulting in:

$$s_L = u_L - M_L \, , \; s_R = u_R + M_R \tag{16}$$

where M_K $(K = L,\, R)$ is given by

$$M_K = \sqrt{(\frac{A_\star \overline{p}_\star}{\rho} - \frac{A_K \overline{p}_K}{\rho})\frac{A_\star}{A_K(A_\star - A_K)}} \tag{17}$$

where $A_\star$ is an estimate for the exact solution of A in the star region. Toro (2001) suggested several estimates for the flow depth in the star region ($y_\star$) in rectangular channels. In appendix B, some of these estimates are extended for a general cross-section channel. The types of non-linear left and right waves are determined by comparing $y_\star$ with the flow depths in the left and right states $[y_K \; (K = L, R)]$. The left or right wave is a shock if $y_\star > y_K \; (K = L, R)$, otherwise the wave is a rarefaction wave (smooth wave). When $A_\star$ is less or equal than $A_K \; (K = L, R)$, it is suggested to replace M_K with the gravity wave celerity $c_K \; (K = L, R)$ given by Eq. 11. The reason is that M_L and M_R are obtained assuming that the star region and the respective constant states are separated by a shock wave. If the star region and the left and right states are connected by a rarefaction wave, the speeds (of the wave heads) of the left and right rarefaction waves are given respectively

by $u_L - c_L$ and $u_R + c_R$ (Toro 2001). Thus, M_K may be expressed as:

$$M_K = \begin{cases} \sqrt{(\frac{A_\star \overline{p}_\star}{\rho} - \frac{A_K \overline{p}_K}{\rho}) \frac{A_\star}{A_K(A_\star - A_K)}} & \text{if } A_\star > A_K \\ c_K & \text{if } A_\star \leq A_K \end{cases} \tag{18}$$

Once the wave speed estimates are computed, the flux at the interface $i + 1/2$ (Equation 15) is fully determined using Equation 2.

Boundary Conditions

In open channel flows there are three flow regimes, subcritical, critical and supercritical, which have their counterparts in compressible flow, namely, subsonic, sonic and supersonic. In subcritical flows, small disturbances propagate upstream and downstream of the location of the perturbation, whereas in supercritical flows, small disturbances only can travel downstream. Thus, it is apparent that if the flow entering the domain is supercritical, two boundary conditions are needed, and if it is leaving the domain, no boundary condition is needed. Likewise, in subcritical flows, if the flow is entering or leaving the domain, only one boundary condition is needed. For instance, in subcritical regime, if a hydrograph (Q *vs* t) is to be prescribed at a boundary, the missing variable may be computed from the generalized Riemann invariants. For the left-hand boundary (interface $i = 1/2$), the generalized Riemann invariants across the wave $dx/dt = u + c$ (Equation 9), or which is the same along the wave $dx/dt = u - c$ (c^-) yield:

$$\frac{Q_{1/2}^{n+1}}{A_{1/2}^{n+1}} - \phi_{1/2}^{n+1} = \frac{Q_1^n}{A_1^n} - \phi_1^n \tag{19}$$

For a general cross section channel, ϕ can be determined approximately by integrating c/A between two successive values of A using any integration technique. Since $A_{1/2}^{n+1}$ and $\phi_{1/2}^{n+1}$ are related, Equation (19) can be solved for $A_{1/2}^{n+1}$. In the case of a circular cross-section channel, $A_{1/2}^{n+1}$ and $\phi_{1/2}^{n+1}$ are functions of the unknown variable θ, and Eq. (19) can be solved for θ by iteration (three or four iterations is usually enough to ensure convergence). The CPU time consumed by this iteration

process represents only a very small fraction of the total CPU time. Knowing θ and consequently $A_{1/2}^{n+1}$ and the prescribed variable $Q_{1/2}^{n+1}$, the flux vector $\mathbf{F}_{1/2}^{n+1}$ at the boundary and at the time level $n+1$ can be computed using Equation (2). Similarly, for the right-hand boundary (interface $i = N + 1/2$), the generalized Riemann invariants across the wave $dx/dt = u - c$ (Equation 8), or which is the same along the wave $dx/dt = u + c$ (c^+) yield:

$$\frac{Q_{N+1/2}^{n+1}}{A_{N+1/2}^{n+1}} + \phi_{N+1/2}^{n+1} = \frac{Q_N^n}{A_N^n} + \phi_N^n \tag{20}$$

When using higher-order schemes, for the quality of the numerical solution to be preserved it is necessary to use a higher-order reconstruction in all the cells. Since common procedures of reconstruction such as MUSCL use one or more cell on each side of the cell to be reconstructed, generally one or more cells are missing within the first and last cells of the computational domain. Typical procedures to handle this problem are based on the implementation of ghost cells outside of the boundaries.

Incorporation of source terms

Similar to Zhao and Ghidaoui (2004), the source terms $\mathbf{S}$ are introduced into the solution through time splitting using a second-order Runge-Kutta discretization which results in the following explicit procedure.

First step (pure advection):

$$\mathbf{U}_i^{n+1} = \mathbf{U}_i^n - \frac{\Delta t}{\Delta x}(\mathbf{F}_{i+1/2}^n - \mathbf{F}_{i-1/2}^n) \tag{21}$$

Second step (update with source term by $\Delta t/2$):

$$\overline{\mathbf{U}}_i^{n+1} = \mathbf{U}_i^{n+1} + \frac{\Delta t}{2}\mathbf{S}\big(\mathbf{U}_i^{n+1}\big) \tag{22}$$

Last step (re-update with source term by Δt):

$$\overline{\overline{\mathbf{U}}}_i^{n+1} = \mathbf{U}_i^{n+1} + \Delta t\mathbf{S}\big(\overline{\mathbf{U}}_i^{n+1}\big) \tag{23}$$

The evaluation of the source terms **S** appearing on Eq. (2) requires the definition of the grid bottom slope $(S_0)_i$ given by

$$(S_0)_i = -\frac{z_{i+1/2} - z_{i-1/2}}{x_{i+1/2} - x_{i-1/2}} = -\frac{\Delta z_i}{\Delta x_i} \tag{24}$$

and the grid energy line slope $(S_f)_i$ which may be obtained from Manning's equation,

$$(S_f)_i = \frac{n_m^2}{{k_n}^2} \frac{\frac{Q_i}{A_i}\left|\frac{Q_i}{A_i}\right|}{R_i^{4/3}} \tag{25}$$

where k_n is 1.0 in Metric units and 1.49 in English units, R is the hydraulic radius and n_m is the so-called Manning roughness coefficient.

Stability constraints

Since the explicit second-order Runge-Kutta discretization has been used for the incorporation of **S** into the solution, the stability constraint must include not only the Courant-Friedrichs-Lewy (CFL) criterion for the convective part, but also the constraint for the source terms. The CFL constraint is given by:

$$Cr_{max} = \frac{\Delta t}{\Delta x_i} \text{ Max }_{i=1,2,\ldots N} \left(|u_i^n| + |c_i^n|\right) \leq 1 \tag{26}$$

where Cr_{max} is the maximum Courant number at time level n. From Eq. (26), the permissible time step for the convective part is given by:

$$\Delta t_{\text{max, CFL}} = \text{Min }_{i=1,2,\ldots N} \left[\frac{\Delta x_i}{|u_i^n| + |c_i^n|}\right] \tag{27}$$

Also, it can be shown that the permissible time step for the source terms ($\Delta t_{max,\mathbf{S}}$) is given by (See appendix C for derivation details):

$$\Delta t_{max,\mathbf{S}} = \text{Min }_{i=1,2,\ldots N} \left[-4\frac{\mathbf{U}_i^{n+1}}{\mathbf{S}(\mathbf{U}_i^{n+1})}, -2\frac{\mathbf{U}_i^{n+1}}{\mathbf{S}(\overline{\mathbf{U}}_i^{n+1})} \right] \tag{28}$$

Since the same time step Δt must be used for the convective part and the source term, $\mathbf{U}_i^n$ must be used instead of $\mathbf{U}_i^{n+1}$. Finally, the maximum permissible time step including the convective part

and the source term will be given by:

$$\Delta t_{max} = \text{Min}_{\ i=1,2,\ldots N} \left[\Delta t_{max,\mathbf{S}},\ \ \Delta t_{\text{max, CFL}} \right] \tag{29}$$

Evaluation of Finite Volume Godunov-type schemes

The purpose of this section is to test the accuracy and efficiency of the two GTS schemes using problems whose solution contain features that are relevant to transient flows in sewers such as shock, expansion and roll waves.

The performance of the GTS methods are evaluated by comparing them to the "Exact" solutions (available only for idealized conditions [e.g., frictionless and horizontal pipes]), "Near exact" solutions, the fixed-grid MOC scheme with space-line interpolation and experimental observations. The "Exact" solution is obtained - at the precision of the computer - with a program written to solve the general Riemann problem for the shallow water equations in circular conduits. The "Near exact" solution is obtained by grid refinement until convergence is achieved. Five tests cases are considered in this section. These are:

(1) Hydraulic bores.

(2) Comparison of accuracy and efficiency among GTS and MOC schemes without friction.

(3) Comparison of accuracy and efficiency among GTS and MOC schemes in presence of friction.

(4) Formation of roll waves.

(5) Hydraulic routing.

In the following sections, for convenience, the maximum Courant number Cr_{max} is denoted by Cr. In addition, the grid size, Courant number, Manning roughness coefficient and channel slope used in each example are indicated in the relevant figures and thus will not be repeated in the text. Furthermore, the CPU times that are reported in this paper were averaged over three realizations

and computed using a Pentium IV 3.20 GHz personal computer.

(1) Hydraulic bores.

The purpose of this test is to demonstrate the capability of the GTS schemes in capturing accurately discontinuities such as hydraulic bores. Hydraulic bores often occur in sewers, particularly after an abrupt change in flow depth or discharge, such as the sudden closure of a downstream gate.

A uniform flow in a 1000 m long frictionless horizontal sewer with a diameter of 2.5 m is considered as the test problem. The initial condition of this problem involves a uniform flow depth ($y = 0.5$ m) and discharge ($Q = 2\ m^3/s$). At time $t = 0$, the supercritical flow is completely blocked at the downstream end of the sewer (e.g., sudden closure of a downstream gate) which generates a bore that travels upstream. The simulation results for the water depth profile at $t = 300$ s are shown in Figure 4. The results show that the moving hydraulic bore is well resolved by both GTS schemes. Furthermore, the execution time of both methods is very similar (0.358 s and 0.353 s for the HLL and Guinot Riemman solvers respectively).

(2) Comparison of accuracy and efficiency among GTS and MOC schemes without friction

This test is used to compare the accuracy and numerical efficiency of the two GTS schemes and the MOC with space-line interpolation without friction. For a given grid size and Courant number, one scheme can be more accurate than another one, but not necessarily more efficient numerically. A comparison of numerical efficiency requires measuring the CPU time needed by each of the schemes to achieve the same level of accuracy (e.g., Zhao and Ghidaoui 2004). The numerical efficiency of a model is a critical factor for real-time control, since small simulation time steps and a large number of grids are needed to reasonably reproduce the formation and propagation of hydraulic transients

in sewer systems.

The test simulates the sudden opening of a gate separating two pools of still water with different depths mid-way in a 1000 m long frictionless horizontal sewer with a diameter of 15 m. Zero water flux boundary conditions are used in the analysis, namely $Q\ (0,t) = 0$ and $Q\ (1000,t) = 0$. The initial conditions are:

$$\begin{cases} y = 10.0\ m \ \text{ and } u = 0.0\ m/s \text{ for } x <= 500\ m \\ y = 3.0\ m \ \text{ and } u = 0.0\ m/s \text{ for } x > 500\ m \end{cases}$$

The ability of the schemes to conserve mass is first tested. Since zero water flux boundary conditions are used in the current test case, the total mass in the sewer is invariant with time. The simulation results for the water depth versus time at $x = 2.5$ m and the mass traces are shown in Figures 5 and 6, respectively. The results show that unlike the MOC scheme, the two GTS schemes conserve mass. For instance, Figure 6 shows that after 400 seconds of simulation, about 20% of the initial total water volume is lost by the MOC scheme and none by the two GTS schemes.

Next, the influence of the Courant number on the accuracy of the schemes before and after the shock and rarefaction waves have interacted with the zero water flux boundaries is investigated. The simulations results are shown in Figures 7, 8 and 9. The results show that for the same Courant number, the numerical dissipation exhibited by the two GTS schemes is significantly smaller than that produced by the MOC scheme. Furthermore, unlike the MOC scheme, the two GTS schemes preserve their resolution for decreasing Courant number. The results also show that the jump simulated by the MOC scheme moves slower than the actual jump. The accurate prediction of the speed of jumps in sewer systems is very important because it dictates the timing at which surcharging occurs.

A quantitative measure of the numerical dissipation can be obtained by using the integral form of the energy equation (Ghidaoui and Cheng 1997). The absence of friction and gravity forces (recall

that in this test case the sewer is assumed to be frictionless and horizontal) and the invariance of the total mass in the sewer with time imply that the total energy is conserved throughout the transient. Therefore, any dissipation found in the results is solely due to numerical dissipation. Figure 10 shows the relative energy traces E_t/E_0 for different Courant numbers. This figure demonstrates that unlike the MOC scheme, the numerical dissipation exhibited by the two GTS schemes is not sensitive to the Courant number. This figure also shows that for a given Courant number, the numerical dissipation produced by the two GTS schemes is significantly smaller than that obtained by the MOC scheme. For instance, when $Cr = 0.3$, after 400 seconds of simulation, more than 40% of the initial total energy is dissipated by the MOC approach and only about 20% by both GTS schemes.

To this point, it is shown that for the same grid size and for the same Courant number, the two GTS schemes are more accurate than the MOC scheme with space-line interpolation. However, as pointed out by Zhao and Ghidaoui (2004), a comparison of numerical efficiency requires measuring the CPU time needed by each of the schemes to achieve the same level of accuracy.

To compare the efficiency of these schemes, before and after the shock and rarefaction waves have interacted with the boundaries (first interaction with the boundaries occurs at about 50 s), the numerical dissipation is plotted against the number of grids on log-log scale and shown in figures 11 and 12. Figure 11 (before the shock and rarefaction waves have interacted with the boundaries) shows that the reduction in numerical dissipation when the number of grids is increased is approximately linear (on log log scale). However, when convergence is close to being achieved, the reduction of the numerical dissipation asymptotically tends to zero. In real-time simulations (due to the computational cost), the accuracy pursued in the numerical modeling will typically fall in the linear portion of Figure 11. Hence, the linear relationships are used for the comparison of numerical efficiency. These linear relationships were fitted to power functions whose equations are

given in Figure 11. These equations were used to compute the number of grids needed by each of the schemes to achieve a given level of accuracy. These in turn were used to compute the CPU times. Accurate estimate of CPU times requires that our model is run for a sufficiently long simulation time. When using 50 seconds simulation time, the CPU time for the GTS schemes is in the order of 10^{-2} seconds. This CPU time is clearly too small to be reliable because the time allocated to uncontrolled processes during the simulation can have a significant impact on small CPU times. Therefore, the simulation time was increased to 10000 seconds, which results in CPU times that are in the order of 1 second. The results for the CPU times for the extended simulation time are presented in Table 1. It is noted that several interactions between the waves and the boundaries occurs during the extended simulation time. The tasks executed at a boundary node are similar to those executed at an internal node (i.e., the efficiency of the scheme is not altered by the interactions at the boundaries). Therefore, the extrapolation remains valid as long as the tasks executed at the boundaries are the same as those at the internal nodes. Notice in Table 1 that the two GTS schemes have similar efficiency. Also note that to achieve the same degree of accuracy, the MOC approach requires a much finer grid size than the two GTS methods. In addition, this table shows that to achieve the specified level of accuracy, the two GTS schemes are about 100 to 300 times faster to execute than the MOC approach.

The results after one wave cycle (Figure 12) show that the accuracy produced by the two GTS schemes cannot be matched by the accuracy of the MOC scheme, even when using a large number of grids. The poor results obtained with the MOC scheme may be explained by recalling that this scheme does not conserve mass. At $t = 0$, the initial total energy (E_0) is only potential. After the flow has reached to a static equilibrium ($t = \infty$), the kinetic energy is zero and the total energy is again only potential. If mass is conserved, the potential energy at $t = \infty$ is 77.1 % of E_0, which means that the maximum energy that can be dissipated in the system is 22.9 % of E_0. Any

additional energy loss is a result of a numerical loss of mass in the simulation. The inability of the MOC scheme to conserve mass can produce dissipations beyond the maximum energy that can be dissipated (22.9 %), as can be observed in Figure 10. In this figure for instance, when Cr = 0.3, after 400 s of simulation time, the MOC scheme has produced a numerical dissipation of more than 40%, about half of which can be attributed to the numerical loss of water mass (Fig. 6). The situation is noticeably improved when the Courant number is increased to a value close to one and a large number of grids is used. However in this particular case, these improvements were not enough to match the accuracy of the GTS schemes.

(3) Comparison of accuracy and efficiency among GTS and MOC schemes in presence of friction

This test is used (1) to investigate and compare the accuracy and efficiency of the two GTS schemes and the MOC method with space-line interpolation in the presence of friction, and (2) to measure the relative magnitude of the numerical and physical dissipation. The parameters for this test case are the same than the previous one except friction is included using a Manning roughness coefficient of 0.015.

Because it is shown that the two GTS schemes have similar accuracy and efficiency, only the GTS scheme with HLL Riemann solver is considered in this test case. Since the energy dissipation in this case is only due to friction (E_f), the total energy (E) after a given period can be obtained by subtracting E_f attained during that period from the initial energy (E_0). E_f may be obtained by integration of the net work done by the force of friction over a given period.

The simulation results for the relative energy traces (E/E_0) for different numbers of grids and Courant numbers is presented in Figure 13. The results for the GTS scheme show that for the same Courant number (e.g., $Cr = 0.3$), the numerical dissipation is slightly reduced when the number of

grids is increased (e.g., 200 instead of 40). Regarding the influence of the Courant number in the solution, it was pointed out previously that the two GTS schemes are not sensitive to this parameter. To determine if the dissipation produced by the GTS scheme is only physical, the traces of 1 - E_f/E_0 and E/E_0 obtained with this scheme with $Cr = 0.9$ and $Nx = 8000$ are compared. Figure 13 shows that these traces are notably different and consequently part of the total dissipation produced by the GTS scheme is numerical. Since numerical dissipation is present, it is expected that the actual physical dissipation produced after a given period will be greater than the value computed for E_f for that period. For instance, after 400 s of simulation time, the computed values of E/E_0 and 1 - E_f/E_0 are approximately 0.80 and 0.93, which means that the total energy dissipation in this example is 20% of the initial energy (E_0). However, the actual physical dissipation is not 7% of the initial energy but a value significantly greater and consequently the numerical dissipation is considerably smaller than 13%.

In the case of the MOC scheme, the results show that for the same number of grids, the dissipation produced is highly dependent on the Courant number. When using a larger number of grids, the numerical dissipation is reduced but not enough to overcome the effect of a small Courant number. The results also show that after the first quarter wave cycle (about 50 s), the accuracy produced by the GTS scheme cannot be matched by the accuracy of the MOC scheme, even when using a Courant number close to one and a large number of grids. In this case, the physical dissipation is totally overwhelmed by the numerical dissipation. The reasons for the poor results obtained with the MOC scheme are similar to those discussed in the previous section.

(4) Formation of roll waves.

The purpose of this test is to demonstrate the ability of the GTS schemes to predict the formation of roll waves. The ability of a model to predict the formation and amplitude of roll waves is important

because these waves constitute one of the instabilities that could lead to sewer surcharging. This instability is related to the friction in the channel bed and is caused mainly by the water moving considerably faster near the free surface than near the bed. Surcharging may occur when the amplitude of these waves is large enough to reach the sewer crown. Even when the amplitude of the roll waves is not high enough to reach the sewer crown, these waves may interact with the air in the gap between the water surface and sewer crown, leading to open channel-pressurized flow instability, which causes surcharging (Ghidaoui 2004).

Linear stability analysis applied to uniform base flow in a very wide channel has shown that the formation of roll waves starts to occur when the Froude number (F) is above 1.5 for the case of the Manning resistance formula. For circular channels this stability critical value is usually greater than 2.0 because of the sidewall effect (Yen 2001).

In a similar way to Zanuttigh and Lamberti (2002), to demonstrate the ability of the GTS schemes to predict the formation of roll waves, the evolution of the periodic perturbation $y' = 0.005 sin(\pi t/2)$ imposed upstream ($x = 0$) over a uniform flow depth y_0 is analyzed. Because it is shown that the two GTS schemes have similar accuracy and efficiency, only the GTS scheme with HLL Riemann solver is considered in this test case. A code developed using the aforementioned GTS scheme was applied to verify if the perturbation is amplified for F higher than about 2.0 and attenuated otherwise. A 500 m long sewer with a diameter of 4 m is considered in the analysis. The range of flows used in the simulations is characterized by Froude numbers between 2.02 and 3.96 and a constant uniform flow depth $y_0 = 1$ m. The wall shear stress is represented using the Manning's equation with a coefficient equal to 0.015, constant along the channel. Since the flow is supercritical, two upstream boundary conditions are required. The first boundary condition is a periodic flow depth ($y_0 + y'$) and the second one is a steady discharge which is computed with the uniform flow parameters. Due to the type of flow regime, at the downstream end a non-reflective boundary condition is specified

to avoid backward reflections into the domain.

The simulation results for the flow depth versus time at the downstream end of the channel ($x = 500$ m) together with the initial perturbation imposed upstream ($x = 0$ m) are presented in Figure 14. This figure, although it does not present characteristics of roll waves (non-symmetric waves with steep fronts), shows that the perturbation is amplified for F higher than about 2.65 and attenuated otherwise. When different periodic perturbations were imposed upstream ($x = 0$), the Froude numbers that dictated whether these perturbations were attenuated or amplified were no longer 2.65, but remained between 2.0 and 3.0. For the tested periodic perturbations, roll waves did not fully develop. A much longer channel (sewer) was needed for the full development of this type of waves. This is due to the fact that roll waves are induced by advective-type instability, where the instabilities grow spatially.

The correct development of the roll waves requires that the frequency of the forcing function at the upstream end be similar to the one for which the flow is least stable. The least stable mode is obtainable from linear stability theory. Such data is not available in this case and it appears that the value of frequency chosen here may not be representative of the least stable mode. One way to deal with this issue is to use a random perturbation. Random forcing at the upstream end subjects the flow to a wide range of perturbation frequencies. The least stable mode grows rapidly with distance downstream and quickly becomes the dominant frequency of the flow and controls the behavior of the roll waves. Random perturbations are investigated below.

The random perturbation used in the analysis is $y' = 0.01 * ran$, where ran is a random number within the range $0 \leq x \leq 1$ generated at every time step. The simulation results for the flow depth versus the longitudinal distance (x) as well as the parameters used in this new simulation are presented in Figure 15. The water waves shown in this figure present the typical characteristics of roll waves. However, the amplitude and speed of these waves may not be accurately predicted

because of the assumptions inherent in the shallow water equations. Recall that the shallow water equations assume that the pressure is hydrostatic, the momentum correction coefficient is equal to one and the wall shear stress during unsteady flow conditions is given by relations that are derived for steady flow conditions. These assumptions are questionable in roll wave flows, where the fluid particles experience significant vertical motion and the velocity profile is far from the steady logarithmic profile. Experimental and theoretical work is required to investigate the importance of the assumptions inherent in the shallow water equations (Ghidaoui 2004).

(5) Hydraulic routing

Most practical engineering problems of unsteady open channel flows involve hydraulic routing. For instance, hydraulic routing simulations are used for determining the attenuation and translation of a flood hydrograph through a stream reach. Given the importance of hydraulic routing in unsteady open channel flow problems, the purpose of this section is to evaluate the performance of the two GTS schemes in solving hydraulic routing problems by comparing the results of the simulations obtained with these methods and experimental observations.

One of the sets of experiments conducted at the Wallingford Hydraulics Research Station (WHRS) in England by Ackers and Harrison in 1964 is considered as the test case. The unsteady flow experiments were performed by introducing prescribed flow hydrographs at the sewer's upstream end after running a steady flow for a period. At the sewer's downstream end, a free overfall was placed to enforce a critical flow at this location. Water stages were measured over time at several locations along the channel. The original data were reported in a paper by Ackers and Harrison (1964) and have been partially reproduced in a number of sources such as Franz and Melching (1997). The Ackers and Harrison paper does not report the values of the experimental data, but includes plots showing scaled data (data collected in 0.25-ft diameter pipe and scaled up to 1-ft diameter pipe

by Froude criterion). Since the original experimental data were not available, the scaled up stage hydrograph is used for comparison here.

The scaled-up data reproduced in Table 2 is routed using both GTS methods. The simulated stage hydrographs are contrasted with the reported scaled experimental observations in Figure 16. As shown in this figure, the performance of both GTS schemes is very similar for all the simulated cases. Furthermore, the execution time of both methods is very similar (8.86 s and 8.72 s for the HLL and Guinot Riemman solvers respectively). In addition, the results show that the stage hydrograph at x = 77.94 m from the upstream end seems to be equally well simulated by both GTS schemes. However at x = 8.66 m from the upstream end, the dispersion shown by the observed stage hydrograph is clearly larger than predicted by both GTS methods, which is specially noticeable on the receding portion of the hydrograph. Franz and Melching (1997) using the so called Full Equations (FEQ) model obtained very similar results to those obtained using the two GTS schemes. They suggest that the discrepancies between simulated and observed values may be due to possible scaling problems and due to the fact that some of the experiments done by Ackers and Harrison included flows in the transition region between laminar and fully turbulent flow, which causes that the roughness coefficient be a function of the Reynolds number.

Conclusions

This work is part of a long term project which aims at developing a hydraulic model for real-time simulation of unsteady flows in sewers ranging from gravity flows, to partly gravity-partly surcharged flows, to fully surcharged flows. The success of this project hinges on the ability of the hydraulic model to handle a wide range of complex boundaries and to provide accurate solutions with the least CPU time. This paper focuses on the development and assessment of two second-order explicit FV-GTS schemes for unsteady gravity flows in sewers, but with no surcharging. Second-order accuracy

in space and time in these schemes is obtained by using MUSCL reconstruction in conjunction with the Hancock two-stage scheme for time integration. The TVD property of both schemes is ensured by applying a pre-processing slope limiter (MINMOD). The local Riemann problem in these schemes is solved by the HLL and Guinot approximate Riemann solvers. The accuracy and efficiency of the two GTS schemes were investigated using problems whose solutions contain features that are relevant to transient flows in sewers such as shock, expansion and roll waves. The key results are as follows:

(1) FV formulation ensures that the two GTS conserve mass and momentum.
(2) The GTS methods handle boundary conditions in a similar way to the MOC scheme.
(3) The MOC scheme with space-line interpolation exhibits increasing numerical dissipation (artificial smoothing of shock fronts) with decreasing Courant numbers. GTS schemes, on the other hand, produce sharp shock fronts even for very low Courant numbers.
(4) Numerical tests show that to achieve a given level of accuracy, the two GTS schemes are significantly faster to execute than the fixed-grid MOC scheme with space-line interpolation, and in some cases, the accuracy produced by the two GTS schemes cannot be matched by the accuracy of the MOC scheme, even when a Courant number close to one and a large number of grids is used.

As it was mentioned in the introduction, a robust and efficient numerical model able to reproduce unsteady gravity flows, unsteady pressurized flows and the simultaneous occurrence of gravity and pressurized flows in sewers was developed by the authors. This model consists of three parts: (1) a pressurized flow model that essentially follows the approach of Zhao and Ghidaoui (2004); (2) a gravity flow model that is described in this paper; and (3) an open channel-pressurized flow interface model that will be described in a subsequent paper.

Acknowledgments

The authors gratefully acknowledge the financial support from the Metropolitan Water Reclamation District of Greater Chicago.

Appendix A

In this appendix, Equations (8), (9) and (10) are derived.

The characteristic form of Equation (6) obtained by expressing the Jacobian matrix of $\mathbf{F}$ with respect to $\mathbf{U}$ is:

$$\frac{\partial \mathbf{U}}{\partial t} + \mathbf{A}\frac{\partial \mathbf{U}}{\partial x} = 0, \quad \text{where } \mathbf{A} = \begin{bmatrix} 0 & 1 \\ c^2 - u^2 & 2u \end{bmatrix}$$

The eigenvalues (λ) and eigenvectors ($\mathbf{K}$) of $\mathbf{A}$ are given by: $\lambda_1 = u - c$, $\lambda_2 = u + c$, $\mathbf{K}_1^T = [1 \;\; u - c]$ and $\mathbf{K}_2^T = [1 \;\; u + c]$, where u is the water velocity and c the celerity of the gravity wave in still water given by Equation (11). These eigenvectors yield the following generalized Riemann invariants:

$$\begin{aligned} \tfrac{dA}{1} &= \tfrac{dQ}{u-c} \text{ across } \tfrac{dx}{dt} = u - c \\ \tfrac{dA}{1} &= \tfrac{dQ}{u+c} \text{ across } \tfrac{dx}{dt} = u + c \end{aligned} \tag{30}$$

The differential relationship across the first wave $dx/dt = u - c$ can be written as $(u - c)dA = dQ$, but since $dQ = udA + Adu$, it can be further simplified to $du + (c/A)dA = 0$, which can be expressed as:

$$du + d\phi = 0 \tag{31}$$

where $\phi = \int (c/A)dA$. For a general cross section channel, ϕ can be determined approximately by integrating c/A between two successive values of A using any integration technique. For a circular cross-section (Fig. 1), ϕ is given by:

$$\phi = \sqrt{g\frac{d}{8}} \int_0^{\theta} \frac{1 - \cos\theta}{\sqrt{(\theta - \sin\theta)\sin(\frac{\theta}{2})}}\, d\theta \tag{32}$$

Since an analytical integration for ϕ has not been found, the expression inside the integral in equation (32) was expressed in series and then integrated from 0 to θ resulting in:

$$\phi = \sqrt{g\frac{d}{8}}\left[\sqrt{3}\,\theta - \frac{\sqrt{3}}{80}\,\theta^3 + \frac{19\sqrt{3}}{448000}\,\theta^5 + \frac{\sqrt{3}}{10035200}\,\theta^7 + \frac{491\sqrt{3}}{27\times 7064780800}\,\theta^9 + ...\right]$$

Integrating Equation (31) across the first wave $dx/dt = u - c$, yields:

$$u_L + \phi_L = u_\star + \phi_\star$$

Similarly, the generalized Riemann invariants across $dx/dt = u + c$ lead to the following relationship:

$$u_\star - \phi_\star = u_R - \phi_R$$

Appendix B

In this appendix, estimates for the exact solution of the hydraulic area in the star region ($A_\star$) are provided. Although the complete solution of the Riemann problem for the one-dimensional shallow water equations involves two variables (e.g., $u_\star$ and $A_\star$), in this appendix, only the estimate for $A_\star$ is provided. The reason is that in the HLL Riemann solver, only an estimate for $A_\star$ is required.

Assuming the two-rarefaction wave approximation, the following estimate for $\phi_\star$ (or equivalently $A_\star$) is obtained from Equations (8) and (9)

$$\phi_\star = \frac{\phi_L + \phi_R}{2} + \frac{u_L - u_R}{2} \tag{33}$$

Since A and ϕ are functions of θ, to determine A, it is required to solve Equation (33) for θ by iteration.

Another relation for $A_\star$ can be obtained by solving the Riemann problem for the linearized hyperbolic system $\partial\mathbf{U}/\partial t + \partial\mathbf{F}(\mathbf{U})/\partial x = 0$ with $\mathbf{F}(\mathbf{U}) \equiv \overline{\mathbf{A}}\mathbf{U}$, $\overline{\mathbf{A}} = \mathbf{A}(\overline{\mathbf{U}})$ and $\overline{\mathbf{U}} \equiv (\mathbf{U}_L + \mathbf{U}_R)/2$. The two eigenvalues for the matrix $\overline{\mathbf{A}}$ are given by: $\overline{\lambda}_1 = \overline{u} - \overline{c}$ and $\overline{\lambda}_2 = \overline{u} + \overline{c}$. The application of the Rankine-Hugoniot condition across the two waves $[\overline{\lambda}_i\ (i = 1, 2)]$ provides the following relation

for $A_\star$:

$$A_\star = \frac{A_R + A_L}{2} + \frac{\bar{A}}{2\bar{c}}(u_L - u_R) \tag{34}$$

where $\bar{A} = (A_R + A_L)/2$ and $\bar{c} = (c_R + c_L)/2$.

Unlike in the case of Equation (33), in Equation (34) no iteration is required to estimate $A_\star$.

Another estimate for $A_\star$ that preserves the simplicity of Equation (34) while adding two important new properties may be obtained based on the depth positivity condition (flow depth is greater than or equal to zero). The added properties are (Toro 2001): (1) it can handle situations involving very shallow water well; and (2) unlike the Riemann solver given in Equation (34) [$u_\star$ is not included], the Riemann solver based on the depth positivity condition is found to be very robust in dealing with shock waves.

In the rest of this Appendix a Riemann solver based on the depth positivity condition is derived:

In Equation (33), enforcing $\phi_\star \geq 0$ leads to the depth positivity condition for the two-rarefaction wave approximation that is a limiting case contained in the exact solution of the Riemann problem.

$$u_R - u_L \leq \phi_R + \phi_L \tag{35}$$

To allow the simple solver given in Equation (34) to have the same depth positivity condition as that of the exact solution of the Riemann problem, Equation (34) is written as:

$$A_\star = \frac{A_R + A_L}{2} + \frac{u_L - u_R}{2\overline{W}} \tag{36}$$

where $\overline{W}$ is a parameter to be determined by enforcing that Equation (36) has the same depth positivity condition as that of the exact solution of the Riemann problem.

Likewise, in Equation (36), enforcing the condition $A_\star \geq 0$ leads to:

$$u_R - u_L \leq \overline{W}(A_R + A_L) \tag{37}$$

The right hand sides of equations (35) and (37) are equal in the dry bed limit ($y_\star = 0$), since

both Riemann solutions (linearized Riemann solver and the one based on the two-rarefaction wave approximation) achieve their limiting value when the flow depth is zero. This condition ensures that the approximate solver (linearized Riemann solver) satisfies the same positivity condition as that of the exact Riemann solution. Hence, comparing the right-hand sides of equations (35) and (37), the parameter $\overline{W}$ is determined as:

$$\overline{W} = \frac{\phi_R + \phi_L}{A_R + A_L} \tag{38}$$

which can be substituted in Equation (36), leading to another estimate for $A_\star$ based on the depth positivity condition;

$$A_\star = \frac{A_R + A_L}{2}\left[1 + \frac{u_L - u_R}{\phi_R + \phi_L}\right] \tag{39}$$

Appendix C

In this appendix, the stability constraint for the source terms is formulated.

The explicit second-order Runge-Kutta procedure involves two discretizations, which are stated by Equations (22) and (23). Equation (22) is subject to the following stability constraint:

$$-1 \leq \frac{\overline{\mathbf{U}}_i^{n+1}}{\mathbf{U}_i^{n+1}} \leq 1 \tag{40}$$

Substituting equation (22) in equation (40), and due to the fact that the time step is always positive, the following relations are obtained:

$$\begin{aligned} \frac{\mathbf{S}(\mathbf{U}_i^{n+1})}{\mathbf{U}_i^{n+1}} &\leq 0 \\ \frac{\mathbf{S}(\mathbf{U}_i^{n+1})}{\mathbf{U}_i^{n+1}}\Delta t &\geq -4 \end{aligned} \tag{41}$$

The first inequality in Equation (41) indicates that, for the solution to be stable, the source term $\mathbf{S}$ must be of opposite sign to the variable $\mathbf{U}$. From the second inequality and taking into consideration the first inequality, the following constraint is obtained:

$$\Delta t \leq -4\frac{\mathbf{U}_i^{n+1}}{\mathbf{S}(\mathbf{U}_i^{n+1})} \tag{42}$$

Similarly, due to the explicit discretization in Equation (23), the following stability constraint is obtained:

$$\Delta t \leq -2\frac{\mathbf{U}_i^{n+1}}{\mathbf{S}(\overline{\mathbf{U}}_i^{n+1})} \tag{43}$$

Thus, the permissible time step for the source term ($\Delta t_{max,\mathbf{S}}$) is given by:

$$\Delta t_{max,\mathbf{S}} = \text{Min}_{\ i=1,2,\ldots N}\left[-4\frac{\mathbf{U}_i^{n+1}}{\mathbf{S}(\mathbf{U}_i^{n+1})}, -2\frac{\mathbf{U}_i^{n+1}}{\mathbf{S}(\overline{\mathbf{U}}_i^{n+1})} \right]$$

Notation

The following symbols are used in this paper:

A =Cross-sectional area of flow;

$\mathbf{A}$ = Jacobian matrix of flux vector;

c = gravity wave celerity;

$\bar{c}$ = average gravity wave celerity;

Cr_{max} or Cr = maximum Courant number;

d = sewer diameter;

E_f = energy dissipation due to friction;

E_t = total energy at time t;

E_0 = total energy at t=0;

$\mathbf{F}$ = Flux vector;

$\mathbf{F}_{i+1/2}^n$ = intercell flux;

F = Froude number;

F_w = momentum term arising from the longitudinal variation of the channel width;

g = acceleration due to gravity;

$\mathbf{K}$ = eigenvector;

k_n = constant equal to 1.0 in Metric units and 1.49 in English units;

l = length of sewer;

M = Mass;

M_K = defined by Eq. 17 or Eq. 18;

M_0 = Mass at t=0;

Nx = Number of grids;

n_m = Manning roughness coefficient;

$\overline{p}$ = average pressure of the water column over the cross sectional area;

Q = discharge;

R = hydraulic radius;

$\mathbf{S}$ = vector containing source terms;

S_f = friction slope;

S_0 = bed slope;

s = wave speed;

t = time;

$\mathbf{U}$ = vector of flow variables;

$\mathbf{U}_i$ = vector of flow variables at node i;

u = water velocity;

$\overline{u}$ = average water velocity;

$\overline{W}$ = defined by Eq. 38;

x = longitudinal coordinate;

y = water depth above channel bottom;

y' = periodic perturbation;

$\overline{y}$ = vertical distance from the sewer invert to the centroid of the hydraulic area;

y_0 = uniform flow depth;

Δt = time step;

Δx = spatial mesh size;

θ = angle of reference;

λ = eigenvalues;

ρ = water density;

$\phi = \int (c/A) dA$

Superscripts

n = computational time level

Subscripts

i = mesh point location in x direction;

L = left state;

R = right state;

$\star$ = star region

References

1. Abbott, M. B., and Minns, A.W. (1997). *Computational hydraulics: Elements of the theory of free surface flows*, Pitman Publishing Limited, London.
2. Ackers, P., and Harrison, A. J. M. (1964). "Attenuation of flood waves in partfull pipes." *Proc. of the Institution of Civil Engineers*, London, 28, 361-382.
3. Alcrudo, F., Garcia-Navarro, P., and Saviron, J-M. (1992). "Flux-difference splitting for 1D open channel flow equations." *Int. J. for Numerical Methods in Fluids*, 14, 1009-1018.
4. Caleffi, V., Valiani, A., and Zanni, A. (2003). "Finite Volume method for simulating extreme flood events in natural channels." *J. Hydraul. Research*, 41(2), 167-177.

5. Chaudhry, M. H. (1987). *Applied hydraulic transients*, Van Nostrand Reinhold, New York.

6. Delis, A. I., Skeels, C. P., and Ryrie, S. C. (2000). "Implicit high-resolution methods for modeling one-dimensional open channel flow." *J. Hydraul. Research*, 38(5), 369-382.

7. Duchesne, S., Mailhot, A., and Villeneuve, J. P., (2004). "Global predictive real-time control of sewers allowing surcharged flows." *J. Envr. Eng.*, 130(5), 526-534.

8. Franz, D. D., and Melching, C. S. (1997). "Full Equations (FEQ) model for the solution of the full, dynamic equations of motion for one-dimensional unsteady flow in open channels and through control structures." *U.S. Geological Survey Water-Resources investigations*, Urbana, Illinois, USA, Report 96-4240.

9. Fujihara M., and Borthwick A. G. L. (2000). "Godunov-type solution of curvilinear shallow water equations." *J. Hydraul. Eng.*, 126(11), 827-836.

10. Ghidaoui, M. S., and Cheng, Y. P. H. (1997). "Energy equation in unsteady open channel flows: Formulation and Application." *Advances in Comput. Eng. Sience*, 582-587.

11. Ghidaoui, M. S. (2004). "Review of sewer surcharging phenomena and models." *Internal technical report, University of Illinois at Urbana - Champaign, USA*.

12. Glaister, P. (1988). "Approximate Riemann solutions of the shallow water equations." *J. Hydraul. Research*, 26(3), 293-306.

13. Godunov, S. K. (1959). "Finite difference methods for the computation of discontinuous solutions of the equations of fluid mechanics." *Math. Sbornik*, 47, 271-306.

14. Guinot, V. (2003). *Godunov-type schemes*, Elsevier Science B.V., Amsterdam, The Netherlands.

15. Hirsch, C. (1990). *Numerical computation of internal and external flows*, Vols. 1 and 2, Wiley, New York.

16. Norreys, R., and Cluckie, I. (1997). "A novel approach to the real-time modeling of large urban drainage systems." *Water Science and Technology*, 36(8-9), 19-24.

17. Sanders, B. F. (2001). "High-resolution and non-oscillatory solution of the St. Venant equations in non-rectangular and non prismatic channels." *J. Hydraul. Research*, 39(3), 321-330.

18. Schilling, W. (1996). "Potential and limitations of real time control." *Proc. 7th International Conference on Urban Storm Drainage*, Hanover, Germany, 803-808.

19. Toro, E. F. (2001). *Shock-capturing methods for free-surface shallow flows*, Wiley, LTD, Chichester, U.K.

20. Tseng, M. H., Hsu, C. A., and Chu, C. R. (2001). "Channel routing in open-channel flows with surges." *J. Hydraul. Eng.*, 127(2), 115-122.

21. Yen, B. C. (1986). *Hydraulics of sewers*, Chapter 1 in Advances in Hydroscience, Urban Storm Drainage, Academic Press, London, Vol. 14, 1-115.

22. Yen, B. C. (2001). *Hydraulics of sewer systems*, in Stormwater collection systems design Handbook, McGraw-Hill.

23. Zanuttigh, B., and Lamberti, A. (2002). "Roll waves simulation using shallow water equations and Weighted Average Flux method." *J. Hydraul. Research*, 40(5), 610-622.

24. Zhao, M., and Ghidaoui M. S. (2004). "Godunov-type solutions for water hammer flows." *J. Hydraul. Eng.*, 130(4), 341-348.

25. Zoppou, C., and Roberts, S. (2003). "Explicit schemes for dam-break simulations." *J. Hydraul. Eng.*, 129(1), 11-34.

Table 1. Comparison of efficiency among the two GTS methods and the MOC scheme with space-line interpolation ($Cr = 0.3$, $t = 10000$ s, $S_f = 0$, $S_0 = 0$) [Nx is number of grids needed to achieve a specified level of accuracy]

Description		HLL	Guinot	MOC
$(E_0 - E)/E_0 = 2\%$	Nx	42	42	1324
	CPU time (s)	2.44	2.55	819.20
$(E_0 - E)/E_0 = 3\%$	Nx	23	22	468
	CPU time (s)	0.83	0.73	104.20

Table 2. Hydraulic characteristics of the scaled-up data from Ackers and Harrison (1964). Used with permission from Institution of Civil Engineers, London

Sewer & inflow characteristics and units	**Scaled-up data values**
Length (m)	304.8000
Diameter (m)	0.3048
Bed slope	0.0010
Roughness height (cm)	0.06096
Manning's n_m (peak flow)	0.0116
Manning's n_m (base flow)	0.0115
Base flow (m^3/s)	0.004984
Peak inflow (m^3/s)	0.018689
Base flow depth (m)	0.0768
Inflow duration (s)	132
Shape of inflow hydrograph	symmetric trapezoid
Duration of peak inflow (s)	12

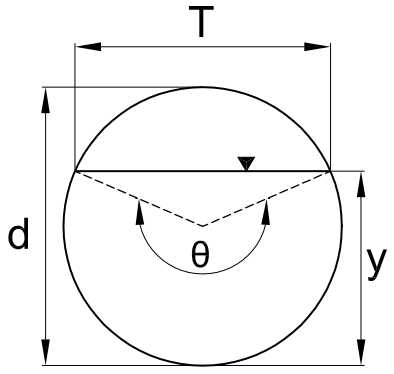

Figure 1. Definition of variables in circular cross-sections

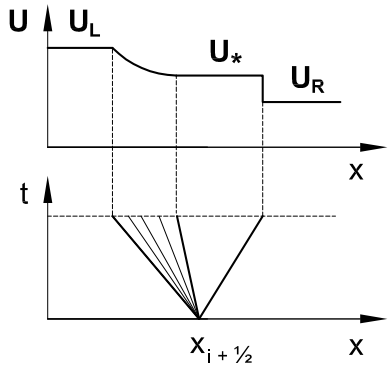

Figure 2. Principle of the Guinot Riemann solver in the physical space (top) and in the phase space (bottom)

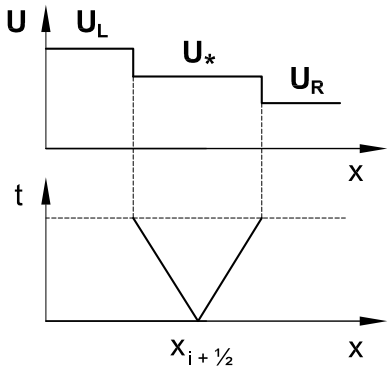

Figure 3. Principle of the HLL Riemann solver in the physical space (top) and in the phase space (bottom)

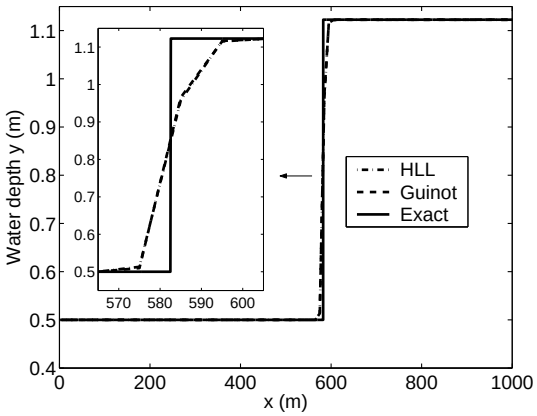

Figure 4. Water depth profile of a hydraulic bore in a sewer generated by complete blockage of the flow at sewer's downstream end ($\Delta x = 10$ m, $Cr = 0.3$, $t = 300$ s, $S_f = 0$, $S_0 = 0$)

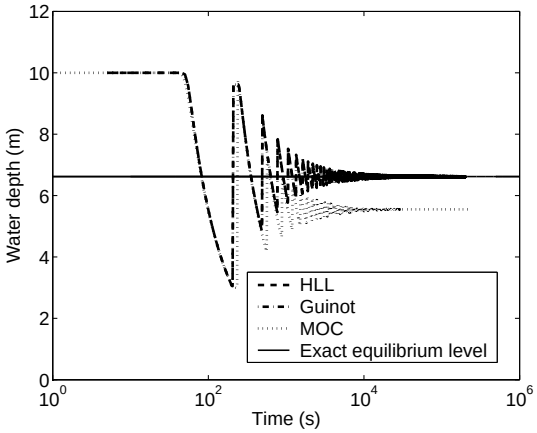

Figure 5. Water depth versus time at $x = 2.5$ m for test No 2 ($\Delta x = 5.0$ m, $Cr = 0.3$, $S_f = 0$, $S_0 = 0$)

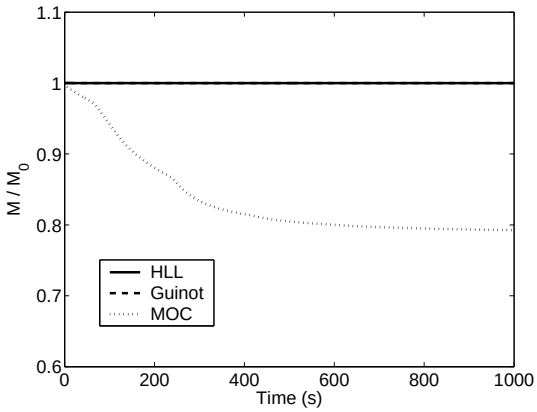

Figure 6. Mass traces for test No 2 ($\Delta x = 5.0$ m, $Cr = 0.3$, $S_f = 0$, $S_0 = 0$)

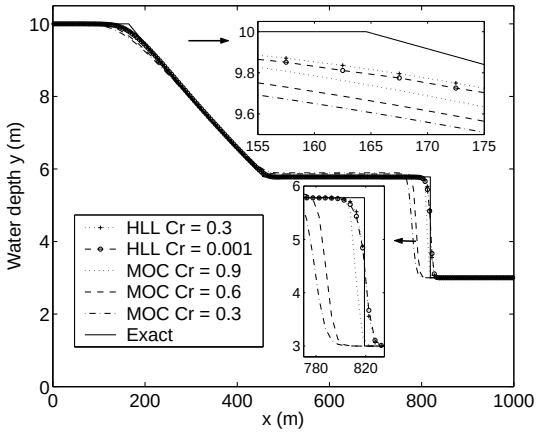

Figure 7. Water depth profile for test No 2 before the shock and rarefaction waves have interacted with the zero water flux boundaries ($\Delta x = 5.0$ m, $t = 36$ s, $S_f = 0$, $S_0 = 0$)

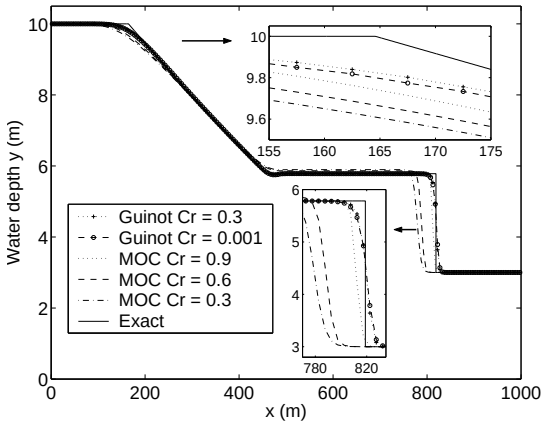

Figure 8. Water depth profile for test No 2 before the shock and rarefaction waves have interacted with the zero water flux boundaries ($\Delta x = 5.0$ m, $t = 36$ s, $S_f = 0$, $S_0 = 0$)

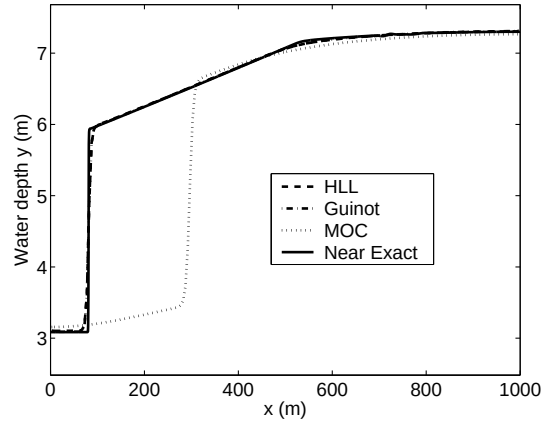

Figure 9. Water depth profile for test No 2 after the shock and rarefaction waves have interacted with the zero water flux boundaries ($\Delta x = 5.0$ m, $Cr = 0.3$, $t = 197$ s, $S_f = 0$, $S_0 = 0$)

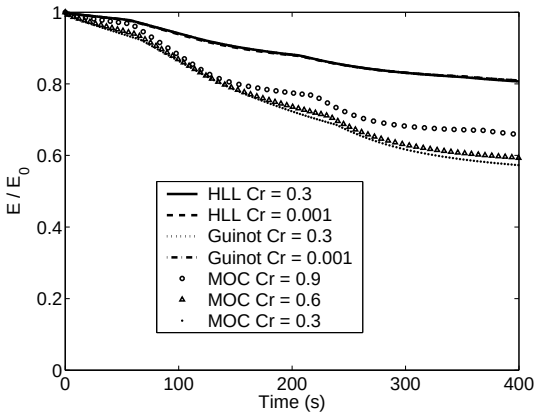

Figure 10. Energy traces for test No 2 ($\Delta x = 5.0$ m, $S_f = 0$, $S_0 = 0$)

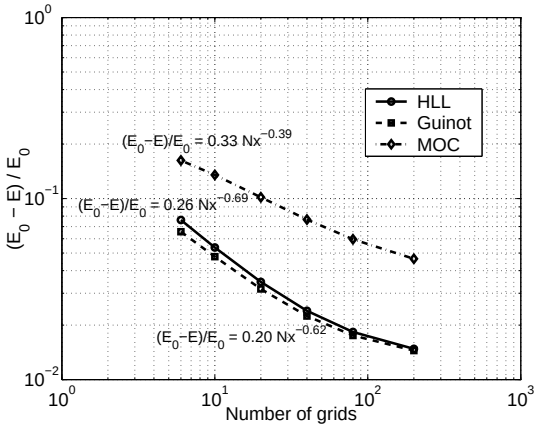

Figure 11. Relation between numerical dissipation and number of grids for test No 2 before the shock and rarefaction waves have interacted with the zero water flux boundaries ($Cr = 0.3$, $t = 36$ s, $S_f = 0$, $S_0 = 0$)

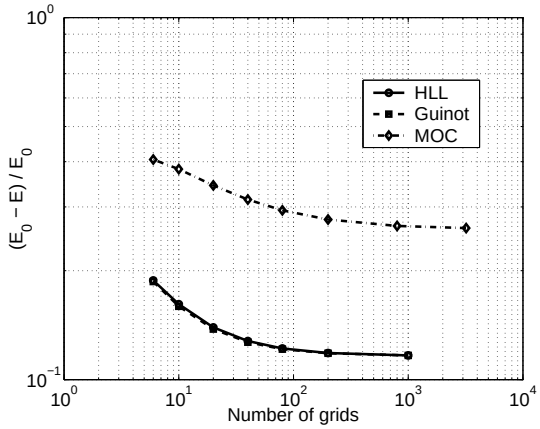

Figure 12. Relation between numerical dissipation and number of grids for test No 2 after one wave cycle ($Cr = 0.3$, $t = 200$ s, $S_f = 0$, $S_0 = 0$)

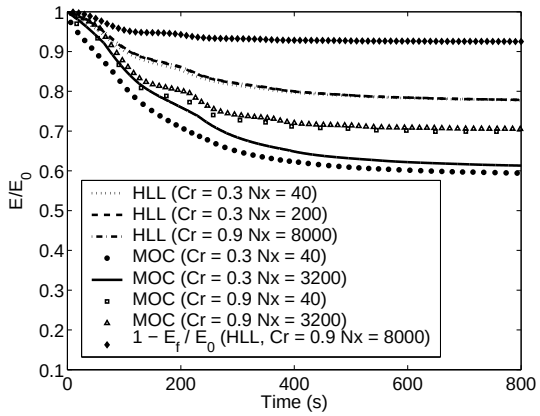

Figure 13. Energy traces for test No 3 ($n_m = 0.015$, $S_0 = 0$)

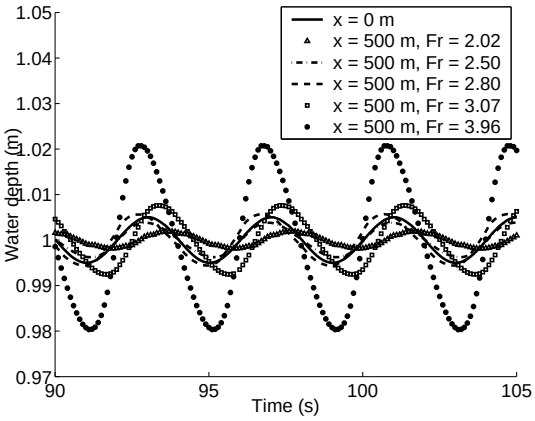

Figure 14. Flow depth versus time at downstream end of sewer ($x = 500$ m) for different Froude numbers together with the perturbation at sewer inlet ($x = 0$ m) [$\Delta x = 0.05$ m, $Cr = 0.8$, $n_m = 0.015$]

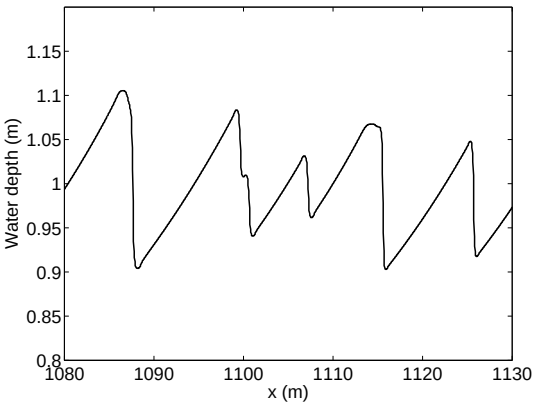

Figure 15. Water depth profile showing typical characteristics of roll waves. [$d = 4$ m, $l = 1200$ m, $\Delta x = 0.04$ m, $Cr = 0.8$, $t = 150$ s, $n_m = 0.015$, $S_0 = 0.10$]

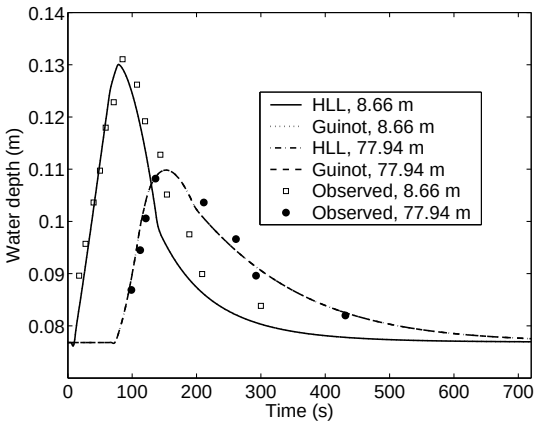

Figure 16. Simulated and observed water depths at $x = 8.66$ m and 77.94 m for scaled sewer pipe ($\Delta x = 1.016$ m, $Cr = 0.3$, $S_0 = 0.001$ and $n_m = 0.0116$) [Experimental data used with permission from Institution of Civil Engineers, London]